Boundary-Layer Meteorology
https://doi.org/10.1007/s10546-020-00520-1

RESEARCH ARTICLE

Friction-Velocity Estimates Using the Trace of a Scalar and the Mean Wind Speed

Francesc Castellví[1] · Kosana Suvočarev[2] · Michele L. Reba[3] · Benjamin R. K. Runkle[4]

Received: 25 October 2019 / Accepted: 26 March 2020
© Springer Nature B.V. 2020

Abstract
A semi-empirical approach based on surface-renewal theory for estimating the friction velocity is tested for measurements taken in the inertial sublayer. For unstable cases, the input requirements are the mean wind speed and the high-frequency trace (10 or 20 Hz) of the air or sonic temperature. The method has been extended to traces of water vapour (H_2O) and carbon dioxide (CO_2) concentrations. For stable cases, the stability parameter must also be considered. The method's performance, taking the direct friction velocity measured by sonic anemometry as a reference, was tested over a growing cotton field that included bare soil with some crop residues at the beginning of the season. In general, the proposed friction-velocity estimates are reliable. For unstable cases, the method shows the potential to outperform the wind logarithmic-law computation. Discarding cases with low wind speeds (e.g., <0.3 m s^{-1} and mean wind shear <1 Hz), the proposed approach may be recommended as an alternative method to estimating the friction velocity. There is the potential, based on the input requirements, that the proposed formulation may offer significant advantages in the estimation of the friction velocity in some marine environments.

Keywords Friction-velocity estimates · Surface-renewal theory · Wind logarithmic law

1 Introduction

The friction velocity u_*, is defined as the shear stress τ_{sh} in units of velocity, $u_* = \sqrt{\tau_{sh}/\rho}$ (where ρ is the air density). Given that the parameter u_* is related to the transfer of momentum towards the surface, its magnitude is conceptually conceived as the degree of friction or drag exerted on the surface by the atmospheric surface layer, and is used to describe the diffusion

✉ Francesc Castellví
francesc.castellvi@udl.cat

1 Department of Environment and Soil Sciences, University of Lleida, Lleida, Spain

2 Department of Land, Air and Water Resources, University of California, Davis, CA 95616, USA

3 United States Department of Agriculture – Agricultural Research Service, Delta Water Management Research Unit, Jonesboro, AR 72401, USA

4 Department of Biological and Agricultural Engineering, University of Arkansas, Fayetteville, AR 72701, USA

and dispersion of particles, tracers, and contaminants, as well as the wind-speed profile near the surface (Stull 1988; Foken 2017). The eddy-covariance (EC) method allows direct measurement of the friction velocity as $u_{*EC} = \left[\left(\overline{u'w'}\right)^2 + \left(\overline{v'w'}\right)^2\right]^{0.25}$, where the overline and prime notations mark the mean and fluctuating parts of the velocity, respectively, after applying Reynolds decomposition (Stull 1988). In the framework of the Monin–Obukhov similarity theory (MOST), the semi-logarithmic wind-speed profile is often used to estimate the value of u_*, which involves the mean wind speed, stability parameter, and canopy parameters (zero-plane displacement d and aerodynamic roughness length z_0) as input. Therefore, the wind-speed logarithmic law and an equation accounting for the buoyant heat flux must be combined to estimate u_*.

Recently, surface-renewal theory (SR) (Higbie 1935; Danckwerts 1951; Harriott 1962; Seo and Lee 1988) combined with the analysis of small eddies in traces measured in the roughness and inertial sublayers (SRSE) has opened new perspectives in micrometeorology. Its applications include the estimation of mass transfer from porous media, such as evaporation from bare soils (Haghighi and Or 2013, 2015), the development of infrared surface anemometers (Aminzadeh et al. 2017), the estimation of the friction velocity over homogeneous and sparse canopies from the mean wind speed and the trace of the air (or virtual) temperature sampled at high frequency, and the estimation of the sensible heat flux (Castellví 2018). The semi-empirical SRSE-based approach to estimating u_* has been tested in both the inertial and roughness sublayers over a variety of agricultural surfaces using temperature traces (Castellví 2018). The objectives of the present work test whether the SRSE approach:

(1) May be applied using other scalar traces than temperature, such as water vapour (H_2O) and carbon dioxide (CO-$_2$) concentration;
(2) Depends on the sampling frequency of the scalar.

In relation to the first objective, we note that to estimate atmosphere–biosphere exchange fluxes of heat and matter, often a gas analyzer and a triaxial sonic anemometer are used without deploying a fine-wire thermocouple (i.e., typically, the buoyancy flux is converted to sensible heat flux following Schotanus et al. 1983). Therefore, an independent approach for estimating u_* using gas traces would benefit when the measurement of the wind field is compromised, for example, following an unexpected physical impact on the triaxial sonic anemometer, such as during its transportation or installation (Zhou et al. 2018). Rainy periods also affect sonic anemometers, but do not affect closed-path infrared analyzers. Additional cases may occur when the flow is distorted by tower mounting, when measurements show a number of spikes, and when deployment heights are too close to the surface, among other reasons (Laurence et al. 1989; Chen et al. 1997a, b; Nakai et al. 2006; Haghighi and Or 2013, 2015; Klipp 2018; Mauder and Zeeman 2018; Peña et al. 2019). In these cases, an estimate of the friction velocity may be useful as an input to many similarity relationships (Stull 1988). In addition, the friction velocity is a key parameter for assessing the near-bed eddy diffusivity for marine environments; this term has been estimated using different approaches, such as the EC method, the dissipation method, the turbulent-kinetic-energy method, and the semi-logarithmic wind-speed profile (Sherwood et al. 2006; Inoue et al. 2011; Johnson and Cowen 2017). Similarly, to estimate the turbulent fluxes of scalars in the benthic sublayer, in some studies, high-frequency measurements were taken of scalars such as temperature and oxygen concentration (Berg et al. 2003). Therefore, the analysis of the friction velocity using the SRSE approach to scalars other than temperature may also be of interest in limnology and marine ecology.

The SRSE approach for estimating the friction velocity assumes that small whirling parcels of air (or eddies, called hereafter 'fluid elements') that originate near the surface are transported up to the roughness and inertial sublayers with little dilution. Therefore, our second objective is to test if the method's performance depends on the size of the fluid elements resolved. For traces of virtual temperature and concentrations of H_2O and $CO\text{-}_2$, the performance was tested for the typical instrumentation frequencies of 10 Hz and 20 Hz.

Overall, we wish to determine if the reliability of the SRSE method in estimating the friction velocity proposed in Castellví (2018) can be reinforced and improved by using different traces and sampling frequencies. In Sect. 2, the SRSE approach is briefly described for estimating the friction velocity when air (virtual) temperature traces and the mean wind speed are available. Here, it is extended to traces of H_2O or $CO\text{-}_2$ concentrations. The field campaign, materials, and methods are given in Sect. 3; the study was carried out over a growing cotton field involving surfaces with different degrees of heterogeneity, including partly-covered bare soil with crop residues during the cotton crop's early growth stages. The results and concluding remarks are given in Sects. 4 and 5, respectively.

2 Theoretical Considerations

2.1 Surface-Renewal Analysis of Small Eddies

The SRSE approach is a semi-empirical method that assumes large descending parcels of air follow a coherent motion and cannot absorb all of the shear exerted near the surface. Consequently, within the volume of the macro-parcel, a population of randomly-distributed fluid elements are generated near the surface (Zhu et al. 2007). During the time that a fluid element remains close to (or in contact with) the viscous boundary layer adjacent to a source (exposure time), the fluid element increases (or decreases) its scalar concentration due to mass (or heat) transfer through the interface until it is randomly replaced by another fluid element. While the macro-parcel of air remains in contact with the surface, these fluid elements tend to homogenize the scalar within its volume and, by continuity (i.e., following a coherent motion), a new descending macro-parcel of air replaces the previous one (Raupach 1981; Paw et al. 1995; Snyder et al. 1996). Most fluid elements remain attached to the replaced macro-parcel of air and, therefore, are ejected upwards (Katul et al. 1996; Zhu et al. 2007). In the SRSE framework, it is assumed that the macro-parcels eject transport fluid elements across finite distances before they have a chance to be dissipated or become significantly diluted.

Actual scalar time traces plotted versus time and measured at some height above the surface (including the inertial sublayer) show small fluctuations embedded in the large ramp-like events, representing the signatures of small eddies superimposed on signatures of coherent structures (Katul et al. 1996; Chen et al. 1997a). An example is shown in Fig. 1 for a trace of the air temperature in unstable conditions. In the SRSE approach, fluctuations are taken as signatures of fluid elements and, as shown in Fig. 1, the ith-fluid-element exposure time with a source of heat τ_i is determined as the time between two consecutive valleys in the trace and its net temperature increases a_i as the difference between the temperature of the peak and of the first valley (Fig. 1). The determination of the period and amplitude of a fluid element's signature has been applied for traces of the wind speed and surface temperature to investigate mass and heat transfer (Haghighi and Or 2013, 2015; Aminzadeh et al. 2017). It is worth mentioning that although in Fig. 1 the signature of a coherent structure has been

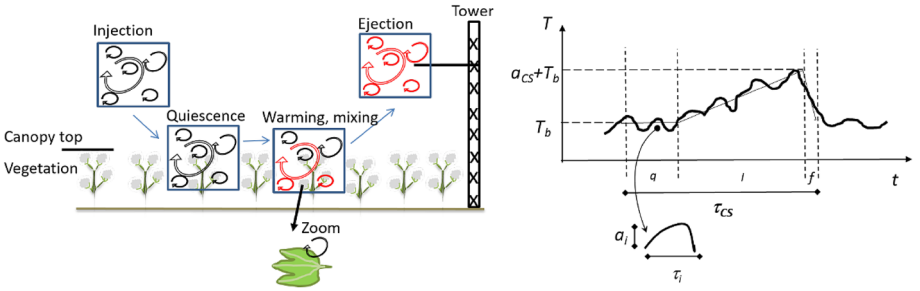

Fig. 1 For an unstable case, the temperature T changes with time t measured at a reference height of a macro-parcel of air following a coherent motion (top left) idealized as a ramp-like shape (thin solid line) with a ramp amplitude a_{CS} and period τ_{CS} (top right) which includes three phases. After a quiescent period q (where T_b is a baseline temperature), the macro-parcel of air (red) is heated during a period l until, by continuity, during a period f, it is replaced by a cooler parcel (blue) coming from above. The actual temperature trace (thick solid line) is composed of the ramp-like shape and small fluctuations associated with signatures of attached fluid elements (bottom left) characterized by a ramp amplitude a_l and period τ_l (bottom right)

idealized following the generalized ramp-like model proposed in Chen et al. (1997a), for the SRSE approach, this abstraction is irrelevant because it focuses on the small fluctuations. Consequently, the concept illustrated in Fig. 1 may adopt any other ramp-like model, such as that proposed by Van Atta (1977) and Shapland et al. (2012), by passing potential issues concerning which ramp model is more realistic.

2.2 Estimation of the Friction Velocity

For temperature traces taken within and above the canopy, Castellví (2018) showed that the probability distribution function (p.d.f.) of the exposure times $PDF_{(\tau)}$ can be modelled by the Gamma distribution (Seo and Lee 1988),

$$PDF_{(\tau)} = \frac{(\alpha+1)^{(\alpha+1)}}{\Gamma_{(\alpha+1)}} \frac{\tau^{\alpha}}{\bar{\tau}^{(\alpha+1)}} \exp\left(-(\alpha+1)\frac{\tau}{\bar{\tau}}\right), \tag{1}$$

where Γ is the gamma function, α (the shape-parameter of the Γ distribution function) is an eddy-spectrum coefficient related to the turbulence intensity (Seo and Lee 1988; Haghighi and Or 2013) and $\bar{\tau}$ is the averaged time exposure. The traditional surface-renewal theory used Eq. 1 for time exposures determined with the wind speed measured at the liquid–gas interface to study heat transfer. For temperature, Castellví (2018) found a linear relationship between the parameters u_* and u/α_T in neutral conditions, which is close to $u_* = ku/\alpha_T$ for measurements taken in the inertial sublayer, where k is the von Kármán constant (= 0.4). To unify the relationship for any height above the canopy and different stability cases, the following semi-empirical approach was proposed to estimate the parameter u_* in the inertial sublayer,

$$u_* = \begin{cases} \frac{k}{\beta_T}\frac{u}{\alpha_T}\phi_m^{-1}(\varsigma) & for\ \varsigma > 0 \\ \frac{k}{\beta_T}\frac{u}{\alpha_T} & for\ \varsigma \le 0 \end{cases}, \tag{2}$$

where β_T is a semi-empirical parameter, u is the mean wind speed, α_T is the shape-parameter determined using temperature traces, and $\phi_m(\varsigma)$ is the momentum stability function for stable cases, where ς is the stability parameter, defined as $\varsigma = (Z-d)/L$, where Z is

the measurement height above the ground, d is the zero-plane displacement, and L is the Obukhov length $L = -\left(\rho C_p T_v / kg\right)(u_*^3 / H_v)$; here, C_p is the isobaric specific heat of the air, H_v is the buoyant heat flux, and T_v is the virtual temperature. The analytical form for the function $\phi_m(\varsigma)$ proposed by Dyer (1974), $\phi_m(\varsigma) = (1 + 5\varsigma)$, was adopted. In Eq. 2, the parameter β_T must be adjusted for neutral cases and is expected to be close to one. Originally (i.e., Castellví 2018), the parameter β_T was denoted as P_{rn} (the turbulent Prandtl number in neutral conditions). However, as pointed out by a reviewer, it is better to use an alternative nomenclature because independent confirmation with concurrent mean scalar gradients is pending (i.e., measurements were available at only one height). For unstable cases, it was suggested to apply Eq. 2 without involving the stability function for the transfer of momentum. It was found that the shape parameterα depends on the stability parameter and the improvement in the friction-velocity estimates was too small to justify the additional complexity.

2.2.1 Scalar Traces Other than Temperature

Given that the analytical form of Eq. 2 is semi-empirical, a generalized equation is proposed for another scalar, such as the H_2O or CO_2 concentration time series,

$$u_* = \begin{cases} \frac{k}{\beta_s} \frac{u}{(\alpha_s + a)} \phi_m^{-1}(\varsigma) & for \varsigma > 0 \\ \frac{k}{\beta_s} \frac{u}{(\alpha_s + a)} & for \varsigma \leq 0 \end{cases}, \tag{3}$$

where the index s denotes the scalar, a is an empirical coefficient, and β_s plays the role of the empirical parameter β_T in Eq. (2).

2.2.2 Parameters β_T and β_s

Though in the inertial sublayer the parameter $\beta_T = 1$ for samples collected in neutral conditions, an equation allowing refinement of the parameters β_T and β_s is of interest and can be obtained unifying the SRSE and the log-law approaches for estimating the parameter u_* in neutral conditions. The generalized logarithmic-law expresses the friction velocity (u_{*WP} where the index WP denotes wind profile) as (Brutsaert 1982)

$$u_{*WP} = \frac{ku}{\ln\left(\frac{Z-d}{z_0}\right) - \Psi\left(\frac{Z-d}{L}\right) + \Psi\left(\frac{z_0}{L}\right)}, \tag{4}$$

where z_0 is the aerodynamic roughness length and Ψ is the integrated Businger–Dyer relationship for momentum to correct for buoyancy. Combining Eqs. 2–4, the following relationship between canopy parameters (d and z_0) and the state of the turbulent flow (through α_T and β_T or α_s and β_s) in neutral conditions holds

$$\ln\left(\frac{Z-d}{z_0}\right) = \begin{cases} \alpha_T \beta_T \\ (\alpha_s + a)\beta_s \end{cases}. \tag{5}$$

Conventional relationships to estimate the parameters d and z_0 for homogenous canopies in agricultural landscapes are (Brutsaert 1982)

$$d = (2/3)h_c, \tag{6}$$

and

$$z_0 = 0.125 h_c, \tag{7}$$

respectively, where h_c is the canopy height. For simplicity, either for traces of H_2O or CO_2 concentration, here it is advanced that the coefficient a in Eq. 3 can be set to unity for typical surfaces in agricultural landscapes (shown in Sect. 4.2). Hence, Eqs. 5–7 enable retrieving the parameters β_T and β_s for homogeneous canopies from

$$\ln\left(\frac{\frac{Z}{h_c}-\frac{2}{3}}{0.125}\right)=\begin{cases}\alpha_T\beta_T\\(\alpha_s+1)\beta_s\end{cases}. \tag{8}$$

3 Materials and Methods

3.1 Field Campaign

The experiment (fully described in Suvočarev et al. 2019) was carried out on a production-sized cotton (*Gossypium hirsutum)* farm in Manila, Arkansas, USA (35° 53′ 14″, − 90° 8′ 15″), from 13 May to 30 September 2016. From the beginning of the campaign until 22 June, bare soil with residue from recently terminated cover crop dominated the field. The row spacing was 0.96 m, and the fraction of ground cover f_c was about 30%. Sparse vegetation predominated from 22 June to 18 July with the canopy height h_c and ground cover in the ranges 0.25–0.90 m and 30–85%, respectively. After 18 July, the crop was considered homogeneous, the value of f_c remained at about 85%, and the maximum canopy height $h_c = 1.10$ m was reached around 28 July. A triaxial sonic anemometer (CSAT3, Campbell Scientific, Logan, Utah, USA.) and an infrared gas analyzer (7500A, LI-COR Biosciences, Lincoln, Nebraska, USA) operating at 20 Hz were deployed at $Z = 3$ m. The mast was situated on a turn-row road (3 m wide) between two fields (45 and 63 ha, 0.1% slope and sprinkler irrigated) to capture flux footprints from both fields. The fields had consistently planted cotton in a radius that varied from 400 m up to 800 m (facing south) from the mast. Thus, although the instrumentation was deployed facing the predominant wind direction (south), the fetch was considered unlimited regardless of the wind direction.

3.2 Database

Following canopy development, three subsets of data were generated that are referred to as 'bare', 'heterogeneous' and 'homogeneous' with samples collected from the beginning of the experiment until 22 June, from 23 June until 18 July, and from 19 July until 30 September, respectively. In addition, given the dependency of Eqs. 6–8 on the canopy height, and of the shape parameter α on the measurement height above the canopy height (Castellví 2018), the heterogeneous dataset was split into three sub-datasets to differentiate periods where the canopy heights were in the ranges 0.3–0.5 m, 0.5–0.7 m, and 0.7–0.9 m. To test a possible frequency dependence, two different datasets were formed for each subset: the original dataset sampled at 20 Hz and one sampled at 10 Hz obtained by skipping every other 0.05-s sample in the 20-Hz series.

3.3 Data Processing

3.3.1 The Eddy-Covariance Method

The mean wind speed was inferred from the triaxial sonic anemometer, and the actual value of u_* was estimated by applying the EC method (u_{*EC}). After correction for flow distortion

by transducer shadowing (Horst et al. 2015), the software package EddyPro 6.2 (LI-COR Biosciences, Lincoln, Nebraska, USA) was used to determine the EC fluxes. The double-rotation method was used for coordinate rotation, and the threshold used for spike detection was set to $\pm 4\,\sigma$, where σ is the standard deviation of values within a 5-min moving window, and 30-min traces were accepted for analysis when no more than 1% of the data was missing. Finally, mean wind directions from behind the sonic anemometer (by $\pm 30°$) were removed to avoid flow distortion by the anemometer's structure and the tower mounting.

3.3.2 Method Based on the Surface-Renewal Analysis of Small Eddies

Basic Quality Control The SRSE and EC methods require a certain degree of turbulent mixing, and the log law may not necessarily work under calm conditions (Livingstone and Warren 1996). A critical threshold to apply flux-variance methods is $u_{*EC} \geq 0.1$ m s^{-1}, with higher thresholds used to ensure quality measurements (Goulden et al. 1996; Gödecke et al. 2004; Dias et al. 2009). From the logarithmic law in neutral conditions,

$$u_* = k(Z-d)\frac{\partial u}{\partial z}, \tag{9}$$

approximating $\partial u/\partial z$ to $u_Z/(Z-d)$ leads to

$$u_* = k u_z, \tag{10}$$

Thus, as a simple quality control for the SRSE approach, samples with $u \leq 0.25$ m s^{-1} are removed.

Shape Parameter α The measured scalar is assumed to consist of coherent and random parts (Van Atta 1977; Katul et al. 1996; Chen et al. 1997a) associated with temperatures of the coherent structure and a fluid element, respectively. To determine the time exposures of the fluid elements (on the order of a few tenths of a second), it was assumed that the change in temperature lagging the sampling time is rather insensitive to the change of the coherent part because ramp periods of coherent structures are of the order of several seconds (highly depending on the surface roughness and stability), and the coherent temperature change is gradual and gentle until the macro-parcel is ejected. When the coherent part of the temperature suddenly drops (Fig. 1), the length of the microfront period is of the order of a tenth of a second (Chen et al. 1997a). Therefore, few measurable fluctuations, if any, are formed using typical frequencies and with time exposures not longer than the sampling period. Here, we note that for simplicity some ramp models have neglected the microfront period (Van Atta 1977; Shapland et al. 2012). Regardless, the SRSE approach avoids identification of coherent ramp dimensions and simply focuses on the determination of time intervals between consecutive valleys along the raw time series (Fig. 1). Once the exposure times in a 30-min scalar trace are determined, the value of α is obtained by fitting Eq. 1 to the actual frequency-distribution function using Brent's root-finding algorithm to minimize the root-mean-square (r.m.s.) error (Brent 1973; Nash 1990). The actual p.d.f. was determined using a bin width of $2/f$, where f is the sampling frequency used (here, 10 Hz or 20 Hz; Sect. 3.2).

3.3.3 Estimates of Canopy Parameters and the parameters β_T and β_s

The zero-plane displacement was neglected for the bare dataset because the cover-crop residue and vegetation were short, sparse, and with a small fraction of ground cover; for the other

datasets, it was estimated using Eq. 6. For each surface, the roughness length is determined by fitting Eq. 4 in neutral conditions

$$u_{*WP_n} = \frac{ku}{\ln\left(\frac{Z-d}{z_0}\right)}, \tag{11}$$

where the index n denotes neutral stability, taking the parameter u_{*EC} as a reference. Given the difficult interpretation of the stability parameter when the sensible heat flux is close to zero (Wang and Brass 2010), the roughness length z_0 was calibrated using samples collected during the negative-to-positive transitions of the sensible heat flux near sunrise and, vice versa, near sunset.

As the proposed coefficient $a = 1$ in Eq. 3 accounts for a mean shift between the shape-parameter α obtained for different scalars (Sect. 4.2), and given the analytical form of Eqs. 2 and 3, separation of variables leads to the expectation that the coefficients β_T and β_s are similar. Therefore, when the zero-plane displacement and the roughness length are difficult to estimate, here it is proposed to set $\beta_T = \beta_s = 0.85$, which is obtained as an intermediate rounded value for the whole campaign (Sect. 4.3) and it is of interest to mention that 0.85 is an intermediate value for the turbulent Prandtl number in neutral conditions in the inertial sublayer (Zilitinkevich et al. 2008; Maronga and Reuder 2017); for homogeneous surfaces, the parameters β_T and β_s are calculated from Eq. 8.

3.4 Performance Evaluation

Here, four friction-velocity estimates are compared with the friction velocity u_{*EC}; three SRSE-derived u_* estimates using different scalar traces and the parameter u_{*WP}. For the log law, u_{*WP} is determined using the calibrated value of z_0 as input.

When the stability parameter is required as input (i.e., for stable cases using the SRSE approach, and for stable and unstable cases using the log law), it was determined using the parameters u_{*EC} and H_{vEC} as input to keep results independent from the method used in the estimation of the buoyancy heat flux. That is, in practice, some traditional method to estimate the sensible heat flux must be implemented to simultaneously solve the friction velocity and the sensible heat flux (Brutsaert 1982; Kustas et al. 1989; Weson et al. 2001; Castellví 2018; Suvočarev et al. 2019). Provided that the mean wind speed and the friction velocity exceed 0.25 m s^{-1} and 0.1 m s^{-1}, respectively, the performance is evaluated by determining the slope and the coefficient of determination R^2 of the linear-regression analysis through the origin and a normalized r.m.s. error. ε as $RMSE/\overline{u_{*EC}}$, where the overbar denotes the u_{*EC} average of all the samples used.

4 Results

4.1 Shape Parameter α

For all three scalars and two sampling frequencies, the actual and theoretical $PDF_{(\tau)}$ are, in general, similar, as shown in Fig. 2. In this example, a sample (14 May at 1730 local time) was recorded under unstable conditions when bare soil predominated, and is selected to show a case with varying source strengths. Regardless of the scalar and sampling frequency, the slope s and coefficient of determination R^2 of the linear regression forced through the origin comparing the actual and theoretical p.d.f. (Fig. 2) are > 0.97 and 0.98, respectively. The

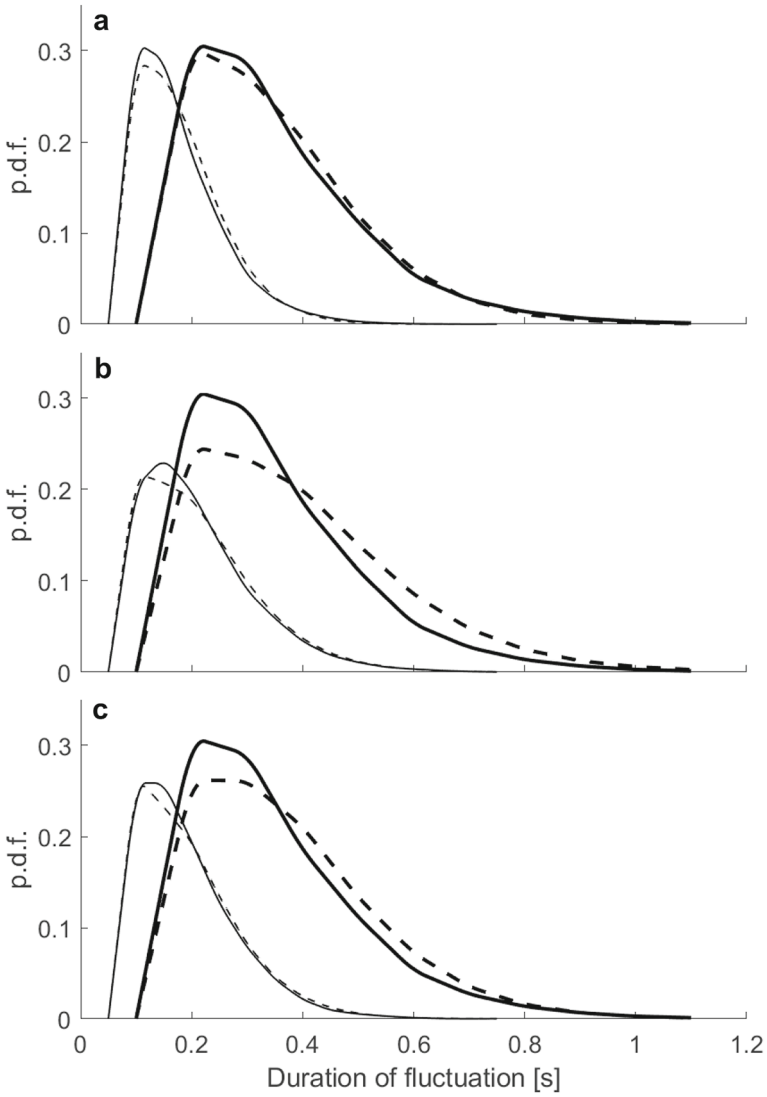

Fig. 2 Actual (solid) and theoretical (dashed) p.d.f. of duration exposure time(referred to as $PDF_{(\tau)}$in the main text) for a 30-min sample (14 May 2016, 1730 local time) collected under unstable conditions over bare soil at 10 Hz (thick) and at 20 Hz (thin) for traces of **a** sonic temperature, **b** water vapour concentration, and **c** carbon dioxide concentration

highest r.m.s. error. obtained was 5×10^{-3} Hz for the H_2O concentration sampled at 10 Hz. The performance obtained for Fig. 2 is consistent and representative for the whole dataset, implying that Eq. 1 fits the observed frequency distribution regardless of the source strength, scalar trace, and sampling frequencies.

For the sample shown in Fig. 2, the number of fluid elements N observed in traces sampled at 10 Hz and at 20 Hz, N_{10}, and N_{20}, using the sonic temperature, H_2O and CO_2 concentrations are (5216, 10,258), (4613, 8485), and (4903, 9376), respectively. Sonic temperature traces

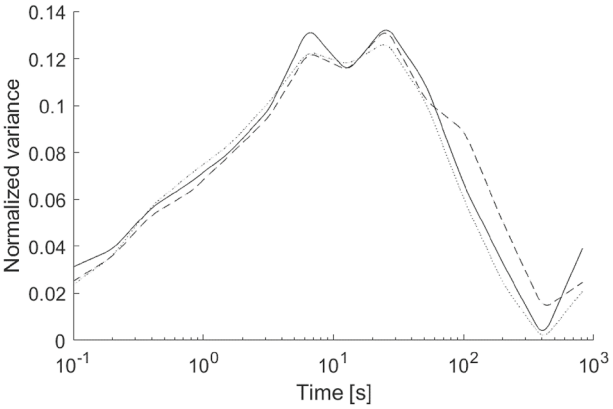

Fig. 3 Multi-resolution decomposition for normalized variances of sonic temperature (solid) and concentrations of water vapour (dotted) and carbon dioxide (dashed). Note the logarithmic time axis

consistently show the highest number of fluid elements across the whole dataset. For traces measured using the gas analyzer, the number of fluid elements observed between both scalars is consistently within 12% across the whole dataset. Regardless of the scalar, the number of fluid elements nearly doubles when the sampling frequency is doubled. As a consequence of the different number of fluid elements observed within a 30-min sample between scalars and sampling frequency, the mean residence time varies and the shape parameter α is mainly dependent on the scalar rather than on the frequency. For the sample shown in Fig. 2, the α values obtained for the sonic temperature α_{Ts}, H_2O concentration α_W and CO_2 concentration α_{CO2} using traces sampled at 10 Hz and 20 Hz are, respectively, 3.82 and 3.91 for the sonic temperature α_{Ts}, 2.85 and 3.01 for the H_2O concentration α_W and 2.82 and 2.96 for the CO_2 concentration α_{CO2}. Thus, regardless of the sampling frequency, the value of α_{Ts} is higher than the α_W and α_{CO2} values, while the α_W and α_{CO2} values are rather similar. For a given scalar, the α_{10} and α_{20} values are similar. Therefore, the results obtained from this sample suggest that Eqs. 2–3 hold for traces sampled at the typical sampling frequencies of 10 Hz and 20 Hz, but that Eq. 2 does not hold for scalars other than temperature. The analytical form of Eq. 3 is analyzed next for all the data.

For the sample shown in Fig. 2, the ramp period of the coherent structures (following Van Atta's 1967 ramp model) is close to 10 s (i.e., for each of the three scalars) and Fig. 3 shows the spectra (time domain) for the normalized variances determined using multi-resolution flux decomposition (Howell and Mahrt 1997; Vickers and Mahrt 2003). The spectra are similar, especially for the smaller eddies, which may be interpreted as suggesting that the higher α value for temperature than for the other scalars (Fig. 2) appears to be a property of the turbulent flow. However, it may not be ruled out that the different volume sampled by the sonic anemometer and the gas analyzer alters the value ofα and enables a closer match between the scalars H_2O and CO_2.

4.1.1 Sampling Frequency

For the heterogeneous dataset, as an example when the crop was growing, Fig. 4 presents the parameters α_{10} and α_{20} for each scalar, demonstrating a similar interval for the sonic temperature (Fig. 4a, b), a broader range for H_2O (Fig. 4c, d), and an even broader range

for the CO_2 concentration (Fig. 4e, f). This performance is also observed for the other two datasets. For each scalar, surface, and stability case, linear regression was used to compare α values determined at 10 Hz and 20 Hz. For the sonic temperature, the values of α_{10} and α_{20} are highly correlated (the minimum R^2 value is 0.88 for the stable cases regardless of the surface). The slope and intercept of the linear regression for the sonic temperature for the highest departures from one and zero, respectively, are 0.83 and 0.71 (both obtained for unstable cases when the surface was homogeneous). For the other two scalars, though correlations are high, the main differences between the parameters α_{10} and α_{20} are observed for extreme values, with the parameter α_{10} underestimating the higher α_{20} values and vice versa (e.g., Fig. 4). This pattern is consistent for all surface types and tends to inflate the intercepts (to positive values) and to force the slopes $s<1$.

For the concentrations of H_2O and CO_2, the worst performance is obtained for stable cases when the canopy is homogeneous using traces of H_2O concentration, corresponding to the smallest coefficient of determination (0.74), the slope with the highest departure from one (0.65), and the intercept with the highest departure from zero (1.17). However, the regression slopes forced through the origin comparing the parameters α_{10} and α_{20} for each dataset are close to one, in the range of 0.94 (stable cases for the 'bare' dataset using traces of the sonic temperature) and 1.09 (unstable cases for the 'heterogeneous' and 'homogeneous' datasets using traces of H_2O concentration). The mean values of the parameters α_{10} and α_{20} are generally similar regardless of the surface, scalar, and stability case.

The weak dependency of the parameter α versus frequency for a particular measurement height in the inertial sublayer was also reported in Haghighi and Or (2015) for the wind-speed parameter α_u. Further research is required to confirm this insensitivity to height, including the roughness sublayer. In addition, these authors found that the value of α_u is linearly related with the quantity $\ln((Z-d)/z_0)$, and thus similar to Eq. 5. A relationship between the parameter α_u and the measurement height is of interest because it has the potential to estimate the boundary-layer depth required to address surface fluxes over bare soils (Haghighi and Or 2013). In future experiments, though it would be of interest to study Eq. 5 for different heights and scalars, here, it is suggested to extend the analysis to the roughness sublayer because the parameter α appears weakly dependent on the measurement height (Castellví 2018).

4.2 Analytical Form of Eq. 3

A different magnitude of α determined using temperature traces measured with the triaxial sonic anemometer is obtained in relation to gas concentration traces measured using the gas analyzer (e.g., Fig. 4). That is, while the shape parameters α_W and α_{CO2} have similar magnitudes, the α_{Ts} term appears shifted, exceeding the values of α_W and α_{CO2} by one or more (Fig. 4). This pattern is consistently observed for the other surfaces, implying that Eq. 2 is not valid for traces measured with a gas analyzer. Therefore, to estimate the friction velocity using gas-concentration traces, a refinement of Eq. 2, such as proposed in Eq. 3, is required. On the basis that the parameter α is weakly dependent on the sampling frequency, an averaged shift $(\alpha_{Ts}-\alpha_s)$ value, is calculated as

$$(\alpha_{Ts}-\alpha_s)=\overline{(\alpha_{Ts}-\alpha_W)_{10}+(\alpha_{Ts}-\alpha_{CO2})_{10}+(\alpha_{Ts}-\alpha_W)_{20}+(\alpha_{Ts}-\alpha_{CO2})_{20}}. \quad (12)$$

This value is 1.12, 1.20, and 1.17 for the 'bare', 'heterogeneous', and 'homogeneous' datasets, respectively. Here, regardless of the sampling frequency, it is proposed to apply Eq. 3 with the rounded value $a=1$. Given that different volumes are sampled using different

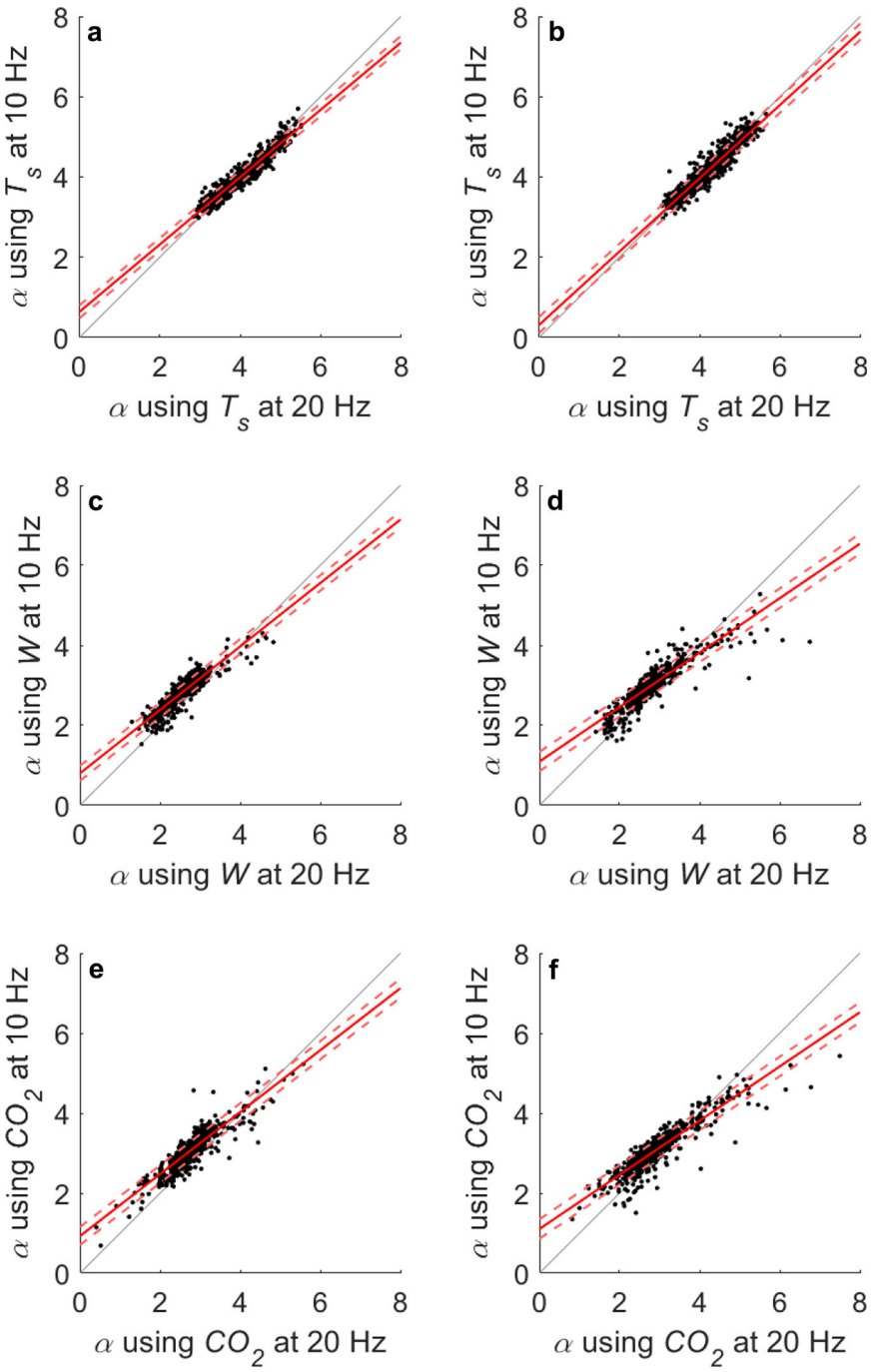

Fig. 4 Shape parameter α determined from 10-Hz (α_{10}) and 20-Hz sampling (α_{20}) in unstable and neutral conditions (left panels; **a**, **c**, **e**) and stable cases (right panels; **b**, **d**, **f**) over a heterogeneous surface. The linear-regression line (red, solid) is accompanied by the standard error of the prediction (red dashed) and the one-to-one line (grey)

Table 1 Calibrated ($z_{0\,\mathrm{cal}}$) and estimated ($z_{0\,\mathrm{Eq.\ 7}}$) roughness lengths z_0 (m) and β_T, β_w, and β_{CO2} estimates retrieved from Eq. 5 (in italics) and Eq. 8 for each surface and scalar

Dataset	N	$Z_{0\,\mathrm{cal}}$	β_T	β_w	β_{CO2}	$Z_{0\,\mathrm{Eq.\ 7}}$	β_T	β_w	β_{CO2}
Bare soil	304	0.05	*0.85*	*1.04*	*0.83*	NA	0.85	0.85	0.85
$h_c = 0.3$–0.5	40	0.06	*0.85*	*1.02*	*0.86*	0.05[a]	0.89	1.06	0.89
$h_c = 0.5$–0.7	34	0.06	*0.79*	*0.98*	*0.88*	0.07	0.76	0.93	0.86
$h_c = 0.7$–0.9	55	0.10	*0.74*	*0.83*	*0.83*	0.10	0.74	0.83	0.83
$h_c = 0.9$–1.1	548	0.135	*0.65*	*0.76*	*0.74*	0.125	0.66	0.78	0.76

N is the number of samples at 10 Hz and 20 Hz together, h_c(m) is the canopy height, and NA denotes non-applicable

[a]Equation 7 not recommended

brands of sonic anemometers and gas analyzers, it may not be discarded that the value for the coefficient a (i.e., $a = 0$ and $a = 1$ for sonic temperature and concentrations of H_20 and CO_2, respectively) would be specific for each instrument.

4.3 Parameter β and the Aerodynamic Roughness Length in Neutral Conditions

For each surface and scalar, Table 1 shows the calibrated roughness z_0, the estimated roughness z_0 from Eq. 7, and the parameter β for the sonic temperature β_{Ts}, the H_2O concentration β_W and the CO_2 concentration β_{CO2} retrieved from both Eq. 5 (i.e., using the calibrated value of z_0 as input and with $a = 1$) and Eq. 8. Following Sect. 4.1.1, the sampling frequency influence on averaged α values is neglected, and therefore, the β values are determined using as input in Eq. 5 or 8 the averaged shape parameter α calculated for both frequencies together. The β values in Eqs. 2 and 3 that best fit the friction velocity u_{*EC} are not shown in Table 1 because, as expected, they closely match the values obtained using Eq. 5 with the calibrated roughness length z_0. The mean value obtained averaging the β_{Ts}, β_W, and β_{CO2} values retrieved from Eq. 5 for all the campaign (Table 1) is 0.84.

For bare soils, Eq. 7 is not applicable and, in general, may be considered uncertain during the initial growing period. However, Table 1 shows that the calibrated z_0 and the estimated z_0 values from Eq. 7 are similar across the entire growing season. Unexpected calibrated z_0 values were obtained when the crop height was around 0.3–0.5 m and 0.5–0.7 m because the value of z_0 is the same for these two datasets, and also when the crop reached the maximum canopy height because the value of z_0 is slightly higher than expected (based on the intermediate value given by Eq. 7). During the period when the canopy height was in the ranges 0.3–0.5 m and 0.9–1.1 m, 32% and 72% of the samples had a mean wind speed $u < 1$ m s^{-1}, respectively. For the other three periods, the percentage of samples with $u < 1$ m s^{-1} is $< 7\%$ each. Partly, the lower data coverage of high-wind-speed periods may explain the unexpected calibrated z_0 values (Livingstone and Warren 1996).

For bare soil, the β values obtained from Eq. 5 show that the assumption of $\beta = 0.85$ regardless of the scalar, is rather reliable for the scalars of temperature and CO_2 concentration, but for H_2O concentration, it is close to one. For CO_2 concentration, the value of β_{CO2} remains fairly constant at around 0.85, except for when the canopy reached the maximum height, for which $\beta_{CO2} = 0.74$. For H_2O concentration, β_w values are approximately one until the canopy height reaches 0.7 m. Afterwards, as the canopy height increased, β_w decreased to reach a similar value ($\beta_w = 0.76$) to that obtained for CO_2 concentration. Thus, Table 1 shows that

Table 2 Friction-velocity estimates determined with traces of temperature (top left) using Eqs. 2 and 8, concentrations of H_2O (top right) and CO_2 (bottom left) using Eqs. 3 and 8, and using the log law (Eq. 5, bottom right) versus the EC method (u_{*EC}) for unstable and neutral cases together and for stable cases

Equation		Equations 2 and 8, T_s						Equations 3 and 8, H_2O					
Case		$\zeta \leq 0$			$\zeta > 0$			$\zeta \leq 0$			$\zeta > 0$		
h_c	N	s	R^2	ε	s	R^2	ε	s	R^2	ε	s	R^2	ε
B.Soil	1024	1.14	0.72	0.32	0.95	0.87	0.22	1.11	0.75	0.28	1.08	0.88	0.26
0.3-0.5	198	1.04	0.80	0.26	1.00	0.89	0.18	1.08	0.87	0.22	0.98	0.92	0.19
0.5-0.7	211	0.95	0.88	0.15	0.98	0.93	0.27	1.00	0.92	0.12	0.96	0.92	0.24
0.7-0.9	176	0.94	0.84	0.23	0.98	0.88	0.13	0.97	0.92	0.15	0.98	0.88	0.15
0.9-1.1	1571	1.06	0.81	0.21	0.95	0.66	0.33	0.97	0.86	0.18	0.93	0.81	0.26
Equation		Equations 3 and 8, CO_2						Equation 5 versus u^*_{EC}					
Case		$\zeta \leq 0$			$\zeta > 0$			$\zeta \leq 0$			$\zeta > 0$		
h_c	N	s	R^2	ε	s	R^2	ε	s	R^2	ε	s	R^2	ε
B. Soil	1024	0.96	0.74	0.23	0.96	0.88	0.21	0.95	0.74	0.23	0.97	0.89	0.20
0.3-0.5	198	0.99	0.85	0.20	0.95	0.92	0.21	1.08	0.83	0.25	1.10	0.92	0.18
0.5-0.7	211	0.95	0.91	0.13	0.95	0.89	0.24	0.95	0.92	0.13	0.97	0.93	0.27
0.7-0.9	176	0.86	0.86	0.25	0.91	0.84	0.17	1.03	0.85	0.24	1.04	0.91	0.12
0.9-1.1	1571	0.95	0.82	0.20	0.93	0.73	0.28	1.09	0.80	0.27	1.03	0.85	0.25

Here, N denotes the number of samples, s and R^2 are the slope and coefficient of determination of the linear-regression analysis, and ε is the normalized root-mean-square error

the value of β_w has the highest variability during the campaign. For virtual temperature, the value of β_{Ts} gradually decreases along the growing season, from 0.85 to 0.65. For the homogeneous dataset, the value of β_{Ts} is 0.65 and for the other two scalars the parameter β is around 0.75. For temperature, β_{Ts} values of about 0.65 appear to be more appropriate for the roughness sublayer (Castellví 2018). Regardless, it is very unlikely that the measurements were consistently taken below the inertial sublayer because $Z/h_c > 2.7$(Florens et al. 2013). In practice, retrieval of parameter β from Eq. 8 prior to application of Eqs. 2–3 is suggested.

4.4 Friction Velocity

For each surface and stability case, Table 2 shows the results of the linear-regression analysis through the origin and the associated error ε to compare the friction velocity u_{*Est} with the values of u_{*WP} and u_{*EC}. The performance for samples collected under neutral and unstable conditions is shown together because the same input is required to determine the value of u_{*Est} (independent from the stability ς). Table 2 shows the performance of Eqs. 2 and 3 using the β values determined from Eq. 8 as input when for a homogeneous canopy (i.e., it is assumed that a triaxial sonic anemometer is not available). However, given the uncertainty of estimating the zero-plane displacement and the roughness sublayer for momentum for bare soil with a partial mulch cover and when the canopy height was 0.3–0.5 m, the parameter β was then set to 0.85 regardless of the scalar. The performance obtained at 10 Hz and 20 Hz is, in practice, the same, so results are shown for the frequency of 10 Hz.

4.4.1 Neutral and Unstable Cases

When bare soil dominates the surface, the best performance for u_{*Est} is obtained for CO_2 concentration, which has a similar performance to u_{*WP}. During the growing period, the performance improves when using traces measured with the gas analyzer rather than the sonic temperature. In fact, using the H_2O concentration, Eq. 3 performed the closest to u_{*EC} (even including u_{*WP}). When the crop tended to reach the maximum fraction of ground cover, either Eqs. 2 and 3 yield values closer to u_{*EC} than u_{*WP}. Therefore, because u_{*WP} gives an optimum friction-velocity estimate (i.e., the input required is determined using sonic anemometry), Table 2 shows that the best performance of the SRSE approach may be expected using a gas analyzer (in particular from traces of H_2O concentration) and that, in general, the SRSE approach and the log law perform similarly.

In relation to the different performance of the SRSE approach for each surface, discarding bare soil, the coefficients of determination for Eqs. 2 and 3 tend to be closer to one for a greater mean shear (u/z, where z denotes the measurement height above the zero-plane displacement) (Table 2). Coherent structures are mainly shear-driven near the surface (Chen et al. 1997b) and the probability to observe $u/z \geq 1$ Hz during bare soil and crop height of 0.3 m $\leq h_c \leq$ 0.5 m, 0.5 m $\leq h_c \leq$ 0.7 m, 0.7 m $\leq h_c \leq$ 0.9 m and 0.9 m $\leq h_c \leq$ 1.1 m is 44%, 39%, 58%, 57%, and 20%, respectively. The SRSE framework best holds for periods (i.e., 30 min) and measurement heights showing clear ramps in traces (Fig. 1). The highest coefficients of determination are obtained during the growing period (Table 2), while lower coefficients of determination are obtained for the bare-soil dataset, implying that the weak source/sink strength associated with bare soil plays a role. In relation to the different performance of the SRSE method for each scalar, given that in general Eq. 3 performs better than Eq. 2, perhaps either the measurement itself plays a role (i.e., gas concentration is a direct measurement) or simply this finding is just a consequence of the semi-empirical nature of the SRSE method.

4.4.2 Stable Cases

The SRSE approach performs similarly regardless of the scalar (Table 2), and both the SRSE approach and the log law yield values close to u_{*EC}. For the whole season, the regression slopes are in a range from 0.93 (Eq. 3 using H_2O and CO_2 concentrations for 0.9 m $\leq h_c \leq$ 1.1 m) to 1.10 (Eq. 5 for 0.3 m $\leq h_c \leq$ 0.5 m). The coefficients of determination are in the range from 0.66 (Eq. 2 for 0.9 m $\leq h_c \leq$ 1.1 m) to 0.93 (Eqs. 2 and 5 for 0.5 m $\leq h_c \leq$ 0.7 m) and ε ranged from 0.12 (Eq. 5 for 0.7 m $\leq h_c \leq$ 0.9 m) to 0.33 (Eq. 2 for 0.9 m $\leq h_c \leq$ 1.1 m). Based on ε along the campaign, the log law yields values consistently somewhat closer to the value of u_{*EC} than for the SRSE method. For stable cases, the calibrated β values (Table 1) are required as input to the SRSE method to nearly match ε obtained from the log law.

To investigate the different performance of the SRSE method for each surface under stable conditions, we take as an example the mean shear threshold of 1 Hz (i.e., the same as for neutral and unstable cases). The probability to observe $u/z \geq 1$ Hz, while the surface is bare soil and the crop height in the ranges 0.3 m $\leq h_c \leq$ 0.5 m, 0.5 m $\leq h_c \leq$ 0.7 m, 0.7 m $\leq h_c \leq$ 0.9 m and 0.9 m $\leq h_c \leq$ 1.1 m is 16%, 26%, 40%, 37%, and 10%, respectively. The highest correlations are obtained during the crop-growth period corresponding to a higher mean shear and vice versa. However, this rule also applied for the bare-soil dataset that yield seven higher correlations than for the homogenous dataset. Here, the above-mentioned potential source/sink strength influence on the performance of the SRSE method still holds because, during the night, all sources or sinks are weak regardless of the surface. Consequently, a clear and regular ramp-like formation in traces is more difficult. In relation to the different

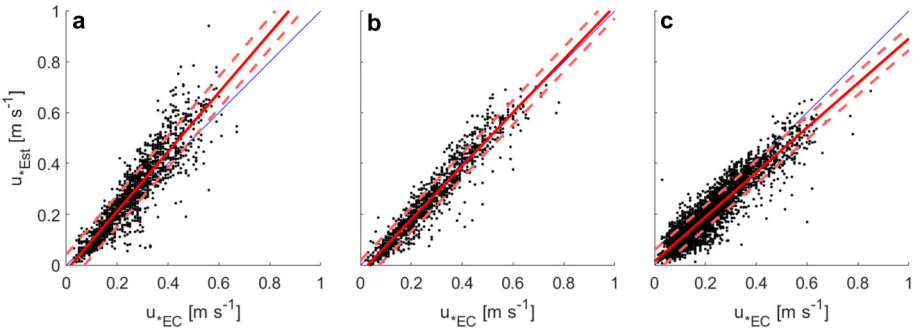

Fig. 5 Friction velocity (Eq. 3 using traces of water vapour concentration) versus u_{*EC} for all the data over **a** partly mulched bare soil, **b** a growing canopy, and **c** a homogeneous canopy. The linear-regression line (red solid) is accompanied by the standard error of the prediction (red dashed) and the one-to-one line (blue)

performance of the SRSE method by scalar, Eqs. 2 and 3 perform similarly, suggesting no dependency on the measured scalar. Therefore, the discrepant performance obtained between Eqs. 2 and 3 can be considered unpredictable since it appears more related with the fact that large ramp events in traces are not well formed in stable stratification.

4.4.3 Applications

As an example of performance through the whole campaign, Fig. 5 shows the performance of Eq. 3 using H_2O concentration traces for each surface. The slopes and the coefficients of determination of the linear-regression analysis and ε obtained for the data shown in Fig. 5 are, respectively, 0.93, 0.98, and 0.26 for the bare-soil dataset, 0.94, 0.92, and 0.18 for the heterogeneous dataset, and 0.89, 0.83, and 0.26 for the homogeneous dataset. In general, these results suggest that use of the SRSE approach for friction-velocity estimates may be recommended and, given that the results are not dependent on the sampling frequency or on the trace of scalar, for field applications, a thermocouple operating at 10 Hz may be considered an affordable method for estimating the value of u_*. An optimal performance can be expected in flow regimes and at measurement heights giving high values of wind shear.

Thus, the SRSE approach appears useful to assess processes requiring a high u_* threshold, such as dust flux or erosion/deposition (Menut et al. 2013). Provided that the mean shear is high (about 1 Hz), the SRSE approach offers a straightforward method to estimate the drag coefficient C_d (Brutsaert 1982) and standard deviations of the turbulent component of the wind speed in neutral conditions (Stull 1988; Pahlow et al. 2001), with

$$C_d = 2(u_*/u)^2 \tag{13}$$

For other stability cases, a similarity-based relationship and Eq. 2 or 3 must be combined with an equation to estimate the sensible heat flux. In addition, it can help to explain the semi-empirical relationship between the mean shear and the mean ramp frequency used for scalar eddy-flux estimates (Chen et al. 1997b). That is, for traces of temperature of the air, good correlations are found between the ratios u_*/z and $1/\tau_{CS}$, so that $u_* = \lambda^z/_{\tau_{CS}}$, where λ is an empirical coefficient. The latter relationship combined with Eq. 2 suggests that part of the observed variability of the coefficient λ with height and surface may be explained by the ratio $k/(\beta_T \alpha)$.

The performance obtained here for different scalars may encourage testing the SRSE approach in studies performed in marine environments. The friction velocity is probably the single most important parameter for assessing the physical characteristics of the benthic boundary layer, and it has profound consequences for the benthic biogeochemistry and ecology (Inoue et al. 2011). It is assumed that similarity-based relationships hold in the inner layer of rough-bed flows covering the lowest 20% of the water depth, provided that the water depth is about ten times higher than the depth of the bed roughness elements. Typically, methods based on normalization of the dissipation rate of the turbulent kinetic energy, involving turbulence intensities or the log law, have been used to estimate the friction velocity assuming neutral stratification in the inertial sublayer (Katul et al. 2002; Pokrajac et al. 2006; Bagherimiyab and Lemmin 2013; Hanmaiahgari et al. 2017). With the formulation proposed, the required inputs may be taken with affordable instruments operating at high frequency, such as a thermocouple or an O_2 microelectrode (Inoue et al. 2011), and deployed at a single height. Therefore, in some marine environments, the SRSE approach appears advantageous over the traditional methods requiring a vertically aligned acoustic Doppler velocimeter, especially when sampling at a few different points is desirable.

5 Summary and Conclusions

This study confirms the reliability of the SRSE method because the analytical form and its performance in estimating the friction velocity are the same and independent from the input trace of the scalar (sonic temperature or concentration of H_2O or CO_2) and sampling frequency (10 Hz or 20 Hz). Except for low wind speeds (e.g., <0.3 m s^{-1} and mean shear <1 Hz), the SRSE approach is as reliable as the log-law approach (or superior under neutral and unstable cases), with the main advantage that it avoids the need to estimate the stability parameter for unstable cases. Hence, provided that the ratio of the mean wind speed over the measurement height (above the zero-plane displacement) is higher than about 1 Hz, and calm conditions (mean wind speeds <0.3 m s^{-1}) are not met, it is concluded that the SRSE method may be considered as a reliable alternative for estimating the friction velocity.

Acknowledgements The authors acknowledge the reviewers' comments that helped to improve this research. Data collection and analysis was partially funded through the US Geological Survey (USGS) under Cooperative Agreements G11AP20066 and G16AP00040 administered by the Arkansas Water Resources Center at the University of Arkansas; the US Department of Agriculture, Natural Resources Conservation Service under Cooperative Agreement 68-7103-17-119, and the National Science Foundation (NSF) under Award 1752083. This work was supported under projects CGL2015-65627-C3-1-R from the Spanish State Research Agency (AgenciaEstatal de Investigación; AEI) and European Regional Development Fund (FondoEuropeo de Desarrollo Regional; FEDER) of the European Union/Unión Europea (AEI/FEDER, UE) and RTI2018-098693-B-C31 from the Ministry of Economy and Competitiveness (Ministerio de Economía y Competitividad) of Spain. The views and conclusions contained in this document are those of the authors and do not represent the opinions or policies of the USGS, NSF, or the Department of Agriculture; mention of trade names or commercial products does not constitute endorsement by any entity.

References

Aminzadeh M, Breitenstein D, Or D (2017) Characteristics of turbulent airflow deduced from rapid surface thermal fluctuations: an infrared surface anemometer. Boundary-Layer Meteorol 165:519–534

Bagherimiyab F, Lemmin U (2013) Shear velocity estimates in rough-bed open channel flow. Earth Surf Process Landf 38:1714–1724

Berg P, Røy H, Janssen F, Meyer V, Jørgensen BB, Huettel M, Beer D (2003) Oxygen uptake by aquatic sediments measured with a novel non-invasive eddy-correlation technique. MEPS 261:75–83. https://doi.org/10.3354/meps261075

Brent RP (1973). Algorithms for minimization without derivatives. Prentice-Hall, Englewood Cliffs, 210 pp

Brutsaert W (1982) Evaporation into the atmosphere. Environmental fluid mechanics. Kluwer Academic Publishers, Dordrecht, 299 pp

Castellví F (2018) An advanced method based on surface renewal theory to estimate the friction velocity and the surface heat flux. Water Resour Res. https://doi.org/10.1029/2018WR022808

Chen W, Novak MD, BlackTA Lee X (1997a) Coherent eddies and temperature structure functions for three contrasting surfaces. Part I. Ramp model with finite micro-front time. Boundary-Layer Meteorol 84:99–123

Chen W, Novak MD, Black TA, Lee X (1997b) Coherent eddies and temperature structure functions for three contrasting surfaces. Part II: renewal model for sensible heat flux. Boundary-Layer Meteorol 84:125–147

Danckwerts P (1951) Significance of liquid-film coefficients in gas absorption. Ind Eng Chem 43(6):1460–1467

Dias N, Hong L, Leclerc MY, Black TA, Nesic Z, Krishnan P (2009) A simple method of estimating scalar fluxes over forests. Boundary-Layer Meteorol 132:401–414. https://doi.org/10.1007/s10546-009-9408-0

Dyer AJ (1974) A review of flux-profile relationships. Boundary-Layer Meteorol 7:363–372

Florens E, Eiff O, Moulin F (2013) Defining the roughness sublayer and its turbulence statistics. Exp Fluids 54(4):1–15

Foken T (2017) Micrometeorology, 2nd edn. Springer, Berlin, 242 pp

Gödecke M, Rebmann C, Foken T (2004) A combination of quality assessment tools for eddy covariance measurements with footprint modelling for the characterization of complex sites. Agric For Meteorol 127:175–188

Goulden ML, Munger JW, Fan FM, Daube BC, Wofsy SC (1996) Measurements of carbon sequestration by long-term eddy covariance: method and critical evaluation of accuracy. Glob Change Biol 2:159–168

Haghighi E, Or D (2013) Evaporation from porous surfaces into turbulent airflows: coupling eddy characteristics with pore scale vapor diffusion. Water Resour Res 49:8432–8442. https://doi.org/10.1002/2012WR013324

Haghighi E, Or D (2015) Linking evaporative fluxes from bare soil across surface viscous sublayer with the Monin–Obukhov atmospheric flux-profile estimates. J Hydrol 525:684–693

Hanmaiahgari PR, Roussinova V, Balachandar R (2017) Turbulence characteristics of flow in an open channel with temporally varying mobile bedforms. J Hydrol Hydromech 65(1):35–48. https://doi.org/10.1515/johh-2016-0044

Harriott P (1962) A random eddy modification of the penetration theory. Chem Eng Sci 17(3):149–154

Higbie R (1935) The rate of absorption of a pure gas into a still liquid during short periods of exposure. Trans AIChE 31:365–388

Horst TW, Semmer SR, Maclean G (2015) Correction of a non-orthogonal, three-component sonic anemometer for flow distortion by transducer shadowing. Boundary-Layer Meteorol 155:371–395. https://doi.org/10.1007/s10546-015-0010-3

Howell FJ, Mahrt L (1997) Multiresolution flux decomposition. Boundary-Layer Meteorol 83:117–137

Inoue T, Glud RN, Stahl H, Hume A (2011) Comparison of three different methods for assessing in situ friction velocity: a case study from Loch Etive, Scotland. Limnol Oceanogr Methods 9:275–287. https://doi.org/10.4319/lom.2011.9.275

Johnson ED, Cowen EA (2017) Estimating bed shear stress from remotely measured surface turbulent dissipation fields in open channel flows. Water Resour Res 53:1982–1996. https://doi.org/10.1002/2016WR018898

Katul GG, Hsieh CI, Oren R, Ellsworth D, Philips N (1996) Latent and sensible heat flux predictions from a uniform pine forest using surface renewal and flux variance methods. Boundary-Layer Meteorol 80:249–282

Katul GG, Wiberg P, Albertson J, Hornberger G (2002) A mixed layer theory for flow resistance in shallow streams. Water Resour Res 38:1250. https://doi.org/10.1029/2001WR000817

Klipp C (2018) Turbulent friction velocity calculated from the Reynolds stress tensor. J Atmos Sci 75:1029–1043. https://doi.org/10.1175/JAS-D-16-0282.1

Kustas WP, Choudhury BJ, Moran MS, Reginato RJ, Jackson RD, Gay LW, Weaver HL (1989) Determination of sensible heat flux over sparse canopy using thermal infrared data. Agric For Meteorol 44(3–4):197–216. https://doi.org/10.1016/0168-1923(89)90017-8

Laurence A, Grant M, Watkins RD (1989) Errors in turbulence measurements with a sonic anemometer. Bound. Layer Meteorol 46(1):181–194. https://doi.org/10.1007/bf00118453

Livingstone I, Warren A (1996) Aeolian geomorphology: an introduction. Addison Wesley Longman Limited, Boston, 211 pp

Maronga B, Reuder J (2017) On the formulation and universality of Monin–Obukhov similarity functions for mean gradients and standard deviations in the unstable surface layer: results from surface-layer-resolving large-eddy simulations. J Atmos Sci 74:989–1010. https://doi.org/10.1175/jas-d-16-0186.1

Mauder M, Zeeman MJ (2018) Field inter comparison of prevailing sonic anemòmetres. Atmos Meas Tech 11:249–263. https://doi.org/10.5194/amt-11-249-2018

Menut L, Pérez C, Haustein K, Bessagnet B, Prigent C, Alfar S (2013) Impact of surface roughness and soil texture on mineral dust emission. J Geophys Res Atmos 118:6505–6520. https://doi.org/10.1002/jgrd.50313

Nakai T, Van der Molen MK, Gash JHC, Kodama Y (2006) Correction of sonic anemometer angle of attack errors. Agric For Meteorol 136:19–30. https://doi.org/10.1016/j.agrformet.2006.01.006

Nash JC (1990) Compact numerical methods for computers: linear algebra and function minimization, 2nd edn. Adam Hilger, Bristol, 278 pp

Pahlow M, Parlange MB, Porté-Agel F (2001) On Monin–Obukhov similarity in the stable atmospheric boundary layer. Boundary-Layer Meteorol 99:225. https://doi.org/10.1023/a:1018909000098

Paw UKT, Qiu J, Su HB, Watanabe T, Brunet Y (1995) Surface renewal analysis: a new method to obtain scalar fluxes without velocity data. Agric For Meteorol 74:119–137

Peña A, Dellwik E, Mann J (2019) A method to assess the accuracy of sonic anemometer measurements. Atmos Meas Tech 12:237–252. https://doi.org/10.5194/amt-12-237-2019

Pokrajac D, Finnigan J, Manes C, McEwan I, Nikora V (2006) On the definition of the shear velocity in rough bed open channel flows. In: Ferreira, Alves, Leal, Cardoso (eds) River flow. Taylor and Francis Group, London

Raupach MR (1981) Conditional statistics of Reynolds stress in rough-wall and smooth-wall turbulent boundary layers. J Fluid Mech 108:363–382

Schotanus P, Nieuwstadt FTM, DeBruin HAR (1983) Temperature measurement with a sonic anemometer and its application to heat and moisture fluctuations. Boundary-Layer Meteorol 26:81–93

Seo YG, Lee WK (1988) Single-eddy model for random surface renewal. Chem Eng Sci 43(6):1395–1402. https://doi.org/10.1016/0009-2509(88)85112-1

Shapland TM, McElrone AJ, Snyder RL, Paw UKT (2012) Structure function analysis of two-scale scalar ramps. Part I: theory and modelling. Boundary-Layer Meteorol 145:5–25

Sherwood CR, Lacy JR, Voulgaris G (2006) Shear velocity estimates on the inner shelf off Grays Harbor, Washington, USA. Cont Shelf Res 26:1995–2018

Snyder RL, Spano D, Paw UKT (1996) Surface renewal analysis for sensible and latent heat flux density. Boundary-Layer Meteorol 77(3–4):249–266. https://doi.org/10.1007/BF00123527

Stull RB (1988) An Introduction to Boundary Layer Meteorology. Kluwer Academic Publishers, Dordrecht, 666 pp

Suvočarev K, Castellví F, Reba ML, Runkle BRK (2019) Surface renewal measurements of H, λE and CO_2 fluxes over two different agricultural systems. Agric For Meteorol 279:107763. https://doi.org/10.1016/j.agrformet.2019.107763

Van Atta CW (1977) Effect of coherent structures on structure functions of temperature in the atmospheric boundary layer. Arch Mech 29:161–171

Vickers FJ, Mahrt L (2003) The cospectral gap and turbulent flux calculations. J. Atmos Ocean Technol 20:660–672

Wang J, Brass RL (2010) An extremum solution of the Monin–Obukhov similarity equations. J Atmos Sci 67(2):485–499. https://doi.org/10.1175/2009jas3117.1

Weson KH, Katul GG, Lai C-T (2001) Sensible heat flux estimation by flux variance and half-order time derivative methods. Water Resour Res 37:2333–2343

Zhou X, Yang Q, Zhen X, Li Y, Hao G, Shen H, Gao T, Sun Y, Zheng N (2018) Recovery of the 3-dimensional wind and sonic temperature data from a sonic anemometer physically deformed away from manufacture geometrical settings. Atmos Meas Tech 11:5981–6002. https://doi.org/10.5194/amt-11-5981-2018

Zhu W, Van Hout R, Katz J (2007) On the flow structure and turbulence during sweep and ejection events in a wind-tunnel model canopy. Boundary-Layer Meteorol 124:205–233

ZilitinkevichS Elperin T, Kleeorin N, Rogachevskii I, EsauI Mauritsen T, Miles M (2008) Turbulence energetics in stably stratified geophysical flows: strong and weak mixing regimes. Q J Roy Meteorol Soc 134:793–799. https://doi.org/10.1002/qj.264

Publisher's Note Springer Nature remains neutral with regard to jurisdictional claims in published maps and institutional affiliations.